Impedance Model-based Stability Analysis of Single-stage Grid-connected Inverters Considering PV Panel Characteristics and DC-side Voltage

Haizhen Xu, Changzhou Yu, *Member*, *IEEE*, Chen Chen, Leilei Guo, Jianming Su, Ming Li, *Member*, *IEEE*, and Xing Zhang, *Senior Member*, *IEEE*

***Abstract*—The rapid and sustained advancement of photovoltaic (PV) power generation technology has introduced significant challenges to the power grid operation, including reduced grid strength and poor damping, thereby causing occurrence of harmonic resonance and potential instability. Conventional stability assessments of PV inverters often overlook critical factors—such as DC-side voltage control and operating mode variations—which arise from the characteristics of the connected PV array. Consequently, these assessments yield inaccurate stability assessments, particularly under weak grid conditions. This study addresses this issue by integrating the characteristics of PV output and DC-side power control into small-signal models while accounting for different control modes, such as constant current (CC), constant voltage (CV), and maximum power point tracking (MPPT). Initially, the study integrates the inverter's output control, LCL filter, and characteristics of the grid to develop a comprehensive framework for the entire PV system. Subsequently, the study uses amplitude and phase stability margins to evaluate how DC-side operating modes, the short-circuit ratio (SCR) of the power grid, and inverter controller parameters influence the system stability. Finally, the accuracy and stability of the model are validated through simulations and a 20-kW three-level prototype PV inverter.**

***Index Terms*—Inverters, photovoltaic systems, stability analysis, PV panel characteristics, DC voltage control.**

Received: July 29, 2024
Accepted: November 30, 2024
Published Online: July 1, 2025

Haizhen Xu, Changzhou Yu (corresponding author), and Chen Chen are with the School of Advanced Manufacturing Engineering, Hefei University, Hefei 230601, China (e-mail: xhzicy@sina. com; ycz87@163.com; chenchen@hfuu.edu.cn).

Leilei Guo is with the College of Electrical and Information Engineering, Zhengzhou University of Light Industry, Zhengzhou 450002, China (e-mail: 2016045@zzuli.edu.cn).

Jianming Su is with the Tongling Power Supply Company of State Grid Anhui Electric Power Co., Ltd., Tongling 244000, China (e-mail: Sujm061X@ah.sgcc.com. cn).

Ming Li and Xing Zhang are with the School of Electrical Engineering and Automation, Hefei University of Technology, Hefei 230009, China (e-mail: liming2021@tsinghua.org.cn; honglf@ ustc.edu.cn).

DOI: 10.23919/PCMP.2024.000197

I. Introduction

The global energy landscape is experiencing a swift transition, driven by an unprecedented rise in renewable electricity generation. Forecasts indicate that by 2026, renewables will comprise nearly 95% of the global power capacity expansion, with solar photovoltaics (PVs) alone contributing over half of this growth [1]. In this evolving landscape, grid-connected inverters are vital interfaces between renewable energy sources and power systems, facilitating efficient energy conversion. Renowned for their high efficiency, swift response, and flexible control, these inverters are increasingly replacing traditional power sources [2]. Positioned near low and medium-voltage distribution networks, they help alleviate electricity consumption pressures, enhance power quality at the grid's edge, strengthen disaster resilience, and ensure dependable power for critical consumers [3].

Nonetheless, the large-scale deployment of inverters in parallel configurations imparts weak-grid characteristics into the power system [4], giving rise to complex phenomena, such as harmonic resonance [3], voltage irregularities [5], and frequency fluctuations [6]. These disturbances often lead to wind and PV curtailment, and in more severe cases, contribute to grid failures. These challenges, in turn, diminish the overall socio-economic benefits of renewable energy generation [7]. Primarily, the large-scale parallel operation of inverters transforms the power grid into a higher-order, time-varying complex network, increasing the risk of coupled resonances among multiple inverters and harmonic amplification due to interactions between grid impedance and renewable energy generation systems [3]. Additionally, a higher penetration level of renewable energy inverters elevates the equivalent impedance perceived by each unit. This phenomenon is particularly exacerbated in remote or rural areas due to long transmission distances and multi-stage voltage transformation stages, which weaken the connections with external grids and result in weak grid characteristics. Consequently, the stability margin of grid-connected inverters with current-source control is reduced, resulting in amplified low-frequency

harmonics in output current and potential instability under extreme conditions [8]. Additionally, the inherent output characteristics of PV arrays necessitate diverse inverter topologies in grid-connected inverters. To maximize the utilization of generated solar power, these inverters may operate under varying control modes, thereby adding complexity to the PV system stability [9].

Various techniques have been proposed for modeling and analyzing the stability of grid-connected converters and their associated systems. While the state-space approach primarily addresses the stability of converter control, its application to distributed systems necessitates accounting for factors such as phase-locked loop (PLL) control and grid impedance, thereby complicating the stability analysis [10]. Alternatively, the impedance-based method—originally proposed by R.D. Middlebrook for assessing the stability of DC-DC converters—has been adapted to evaluate the interaction stability between converters and power grids [11]. This approach models the converter and power grid as in-dependent subsystems using Thevenin or Norton equivalent circuits to capture their external behaviors. Subsequently, open-loop Bode plots or Nyquist criteria are utilized to assess the interactional stability between these subsystems [12]. Building upon this foundation, harmonic linearization using positive- and negative-sequence impedances has gained prominence for its clear physical interpretation. Additionally, impedance can be directly measured through simulations or experimental setups to validate model accuracy [13], [14]. However, due to asymmetries in DC-side voltage regulation, PLLs, and coordinate transformations, grid-connected inverters exhibit significant nonlinear characteristics that lead to frequency coupling phenomena, thereby adversely affecting system-level stability [15], [16]. In [17], a two-stage PV grid-connected inverter is analyzed, wherein the front-end and back-end stages are modeled separately, without providing an integrated small-signal model, thereby limiting comprehensive analysis of the overall system stability.

To achieve accurate stability analysis and elucidate the effect of frequency coupling on inverter stability, in [18]–[19], PLL control is integrated into the positive and negative sequence impedance matrices for grid-connected inverters, thereby improving model accuracy. In [18], it is shown that under weak grid conditions, the PLL's negative impedance characteristics interact with grid impedance, potentially affecting inverter stability due to low-order voltage harmonics. In [20], an adaptive method for controlling PLL band-width is proposed, which reduces the bandwidth as grid impedance increases to preserve system stability. The influence of DC-side voltage control loops was further considered in the derivation of sequence impedance matrices [21]–[23]. In [21], the impact of various current controllers on system stability is examined; however, it did not explore the effects of voltage loop control on system stability. In [22], the role of DC-side voltage loop control in shaping the frequency coupling characteristics within the system is analyzed. In [23], the generalized Nyquist criterion is further utilized to emphasize the importance of DC-side voltage control for the stability of grid-connected converters. However, these modeling and analysis techniques rely on strong-grid assumptions and fail to address the impact of DC-side voltage control on stability under weak-grid conditions.

This study investigates and establishes a small-signal model for a single-stage grid-connected PV inverter, with integrated DC-side voltage regulation. The model incorporates various DC-side operating modes determined by the characteristics of the PV module. Subsequently, the impacts of short-circuit ratio (SCR), DC-side operating modes, and variations in regulator parameters on system stability are analyzed. To validate the proposed model and its dynamic analysis, a 20-kW experimental and simulation platform for the PV inverter is established. The main contributions of this study are outlined as follows:

1) A small-signal model for a single-stage PV grid-connected inverter is developed, incorporating DC-side voltage control. This study analyzes how variations in regulator parameter gains within both the DC voltage and AC current control loops affect system stability, particularly under weak grid conditions.

2) Based on the characteristics of the PV array, the inverter's DC-side control is designed to support multiple operating modes, including constant voltage (CV) mode, constant current (CC) mode, and maximum power point tracking (MPPT) mode that operates between CV and CC modes—based on the PV array characteristics. This paper investigates system stability across different operating modes under weak grid conditions.

3) Experimental results and simulations are performed to validate the proposed model with integrated DC-side control and to confirm its stability under diverse operating modes.

II. Modelling of Grid-connected PV Inverter with DC Control

A. Structure and Working Principle of PV Inverter

The architecture of string PV inverters typically adopts a transformerless three-level topology, as shown in Fig. 1 [3], [24]. A T-type configuration for the three-phase bridges features a shared DC bus with bus capacitors C_{bus}, creating equal positive and negative capacitances. The midpoint of this configuration connects to the inverter's neutral point. The AC output comprises three phases—A, B, and C—filtered through

an LCL-type configuration to suppress switching frequency harmonics and preserve the integrity of the waveform. This filter comprises the inverter-side inductor L_1, the filter capacitors C_1/C_2, and the grid-side inductor L_2. Connecting the midpoint of C_1 to the DC bus midpoint reduces the common-mode current in the output [24]. The inverter's output, termed as the point of common coupling (PCC), connects to the grid, modeled as an ideal AC voltage source E_g in series with grid impedance Z_g. For protection and control, the AC current sampling point $i_{L1\_a(bc)}$ is positioned at the inverter-side output. Due to the low inductance of inductor L_2 and the control-oriented decoupling of the LCL filter into an L-type filter, the AC voltage sampling point $v_{C1\_a(bc)}$ is placed at the filter capacitor.

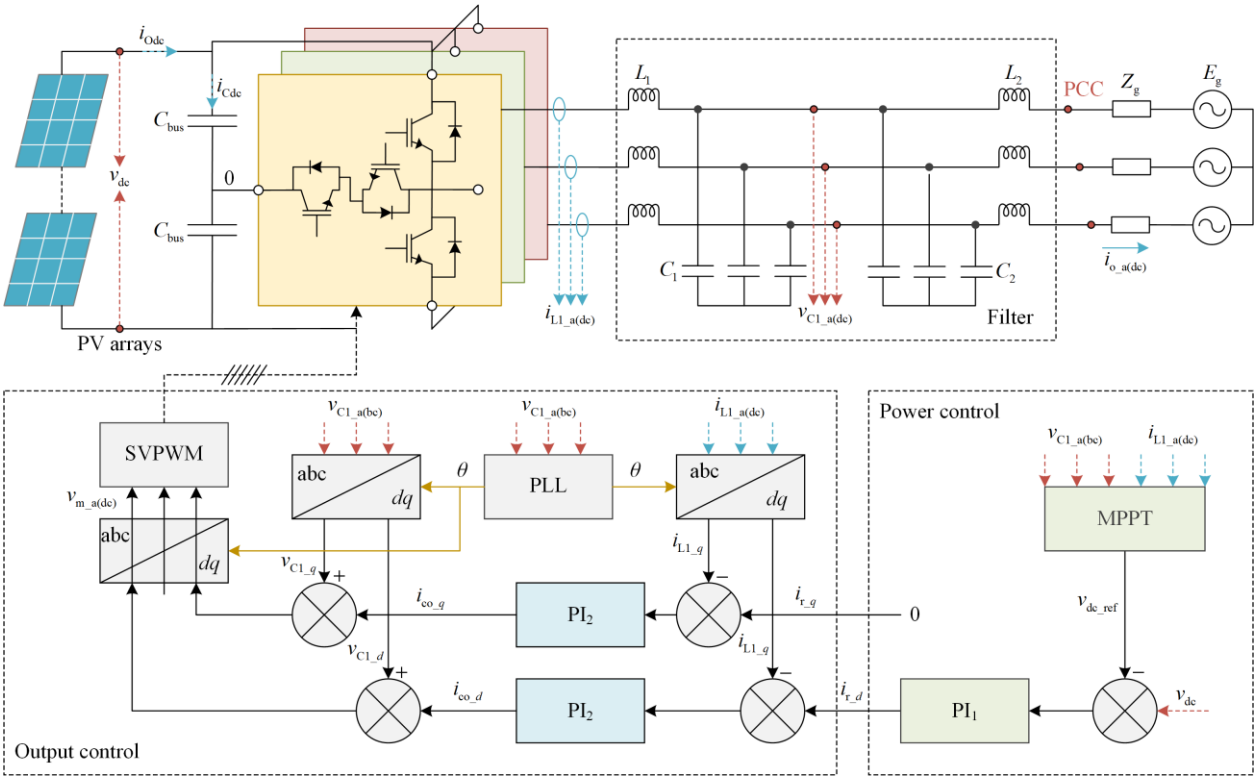

Fig. 1. Hardware structure of grid-connected PV inverter.

The control strategy for the grid-connected PV inverter comprises two main objectives: regulating the DC-side voltage and controlling the AC-side current, as depicted in Fig. 1. The MPPT algorithm is tasked with calculating the DC-side voltage reference, v_{dc_ref}, by evaluating both real-time and historical power data. The DC voltage control loop utilizes v_{dc_ref} as a reference point, comparing it with the actual sampled voltage, (v_{dc}). A proportional-integral (PI) regulator, $PI_1(R_{PI1})$, then regulates the error to generate the AC current references, i_{r_d} and i_{r_q}, within the rotating dq frame. Simultaneously, the AC current control loop references i_{r_d} and i_{r_q}, comparing them with the rotationally transformed inverter-side inductor currents, i_{L1_d} and i_{L1_q}. The resulting feedback from these currents informs the output of a second PI regulator, $PI_2(R_{PI2})$, which generates the control signals i_{co_d} and i_{co_q} to ensure precise current tracking. Before the pulse width modulation (PWM) signal synthesis, the dq frame capacitor voltages, v_{C1_d} and v_{C1_q}, are combined with the PI_2 controller outputs, i_{co_d} and i_{co_q}. The resulting signals then undergo an inverse rotational transformation to yield the PWM inputs. The requisite phase information for these transformations is obtained via a PLL synchronized to the grid voltage, $v_{C1\_a(bc)}$, ensuring synchronization with the grid's voltage waveform [25].

B. Small-signal Modeling of PV Inverter

The small-signal model of the grid-connected inverter is defined in the rotating dq domain and comprises three components: the control plant, the power control, and the output control, as illustrated in Fig. 2.

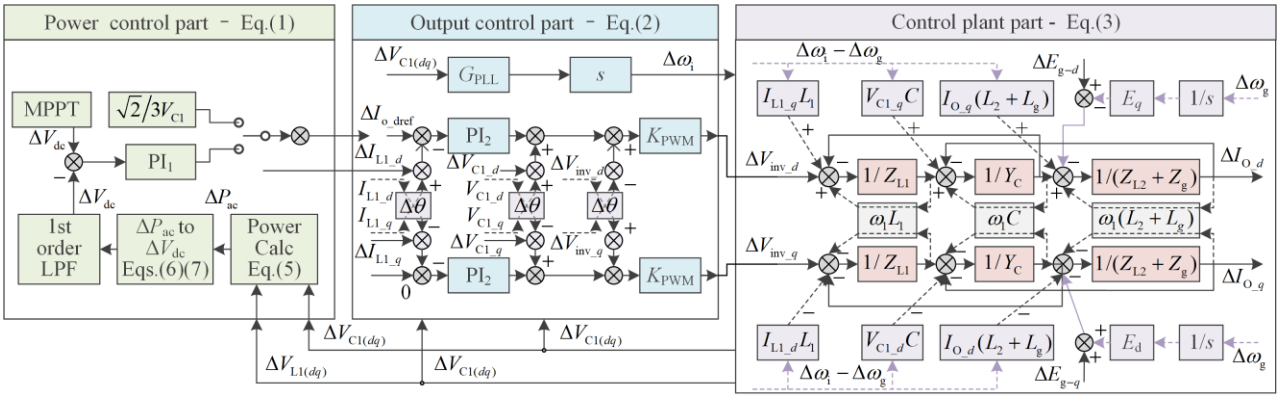

Fig. 2. Diagram of framework of the overall system model.

The corresponding mathematical formulations for each component are shown in (1), (2), and (3). The regions above and below the dashed line in the figure highlight distinct control modes, which are further explained below.

$$\begin{bmatrix}\Delta I_{\mathrm{O\_}d\mathrm{ref}}\\ \Delta I_{\mathrm{O\_}q\mathrm{ref}}\end{bmatrix}=\boldsymbol{G}_{\mathrm{CP1}[2\times6]}\begin{bmatrix}\Delta I_{\mathrm{C1}(dq)[2\times1]}\\ \Delta I_{\mathrm{O}(dq)[2\times1]}\\ \Delta I_{\mathrm{L1}(dq)[2\times1]}\end{bmatrix}+\frac{\boldsymbol{G}_{\mathrm{CP2}[2\times1]}\Delta V_{\mathrm{dcref}}}{\boldsymbol{G}_{\mathrm{CP2}[2\times1]}\Delta P_{\mathrm{cref}}} \quad (1)$$

$$\begin{bmatrix}\Delta\omega_{\mathrm{i}}\\ \Delta V_{\mathrm{inv}(dq)[2\times1]}\end{bmatrix}=\boldsymbol{G}_{\mathrm{CI1}[3\times6]}\begin{bmatrix}\Delta V_{\mathrm{C1}(dq)[2\times1]}\\ \Delta I_{\mathrm{O}(dq)[2\times1]}\\ \Delta I_{\mathrm{L1}(dq)[2\times1]}\end{bmatrix}+\boldsymbol{G}_{\mathrm{CI2}[3\times2]}\begin{bmatrix}\Delta I_{\mathrm{O\_}d\mathrm{ref}}\\ \Delta I_{\mathrm{O\_}q\mathrm{ref}}\end{bmatrix} \quad (2)$$

$$\begin{bmatrix}\Delta V_{\mathrm{C1}(dq)[2\times1]}\\ \Delta I_{\mathrm{O}(dq)[2\times1]}\\ \Delta I_{\mathrm{L1}(dq)[2\times1]}\end{bmatrix}=\boldsymbol{G}_{\mathrm{LC1}[6\times3]}\begin{bmatrix}\Delta\omega_{\mathrm{i}}\\ \Delta V_{\mathrm{inv}(dq)[2\times1]}\end{bmatrix}+\boldsymbol{G}_{\mathrm{LC2}[6\times3]}\begin{bmatrix}\Delta\omega_{\mathrm{g}}\\ \Delta E_{\mathrm{g}(dq)[2\times1]}\end{bmatrix} \quad (3)$$

1) Control plant part. This segment comprises the LCL filter and the grid. It receives input variations in the grid voltage amplitude, $\Delta E_{\mathrm{g}(dq)}$, grid frequency, $\Delta\omega_{\mathrm{g}}$, inverter output voltage, $\Delta V_{\mathrm{inv}(dq)}$, and inverter frequency, $\Delta\omega_{\mathrm{i}}$. The outputs are the inverter's control state variables: $\Delta I_{\mathrm{L1}(dq)}$, $\Delta V_{\mathrm{L1}(dq)}$, $\Delta V_{\mathrm{C1}(dq)}$, and $\Delta I_{\mathrm{O}(dq)}$. The corresponding small-signal block diagram of this section is shown in Fig. 2 [14], where Z_{L1}, Y_{C}, Z_{L2}, and Z_{g} represent the impedances of components L_{1}, C, L_2, and L_{g}, respectively. The capitalized variables in Fig. 2 represent the steady-state operating points of the corresponding parameters in Fig. 1; each parameter preceded by a "Δ" symbol is a small signal increment based on steady-state operating points. The steady-state current amplitudes on the grid side and the inverter side are respectively denoted as $I_{\mathrm{L1\_}d}$, $I_{\mathrm{L1\_}q}$ and $I_{\mathrm{O\_}d}$, $I_{\mathrm{O\_}d}$, while $V_{\mathrm{C1\_}d}$ and $V_{\mathrm{C1\_}q}$ represent the steady-state voltages across the filter capacitors. The segment's input-output relationship is defined as follows:

$$\boldsymbol{G}_{\mathrm{LC1}[6\times3]}=\begin{bmatrix}\boldsymbol{M}_{\mathbf{1}[2\times1]} & \boldsymbol{M}_{\mathbf{2}[2\times2]}\\ \boldsymbol{M}_{\mathbf{5}[2\times1]} & \boldsymbol{M}_{\mathbf{6}[2\times2]}\\ \boldsymbol{M}_{\mathbf{9}[2\times1]} & \boldsymbol{M}_{\mathbf{10}[2\times2]}\end{bmatrix},\quad \boldsymbol{G}_{\mathrm{LC2}[6\times3]}=\begin{bmatrix}\boldsymbol{M}_{\mathbf{3}[2\times1]} & \boldsymbol{M}_{\mathbf{4}[2\times2]}\\ \boldsymbol{M}_{\mathbf{7}[2\times1]} & \boldsymbol{M}_{\mathbf{8}[2\times2]}\\ \boldsymbol{M}_{\mathbf{11}[2\times1]} & \boldsymbol{M}_{\mathbf{12}[2\times2]}\end{bmatrix} \quad (4)$$

In equation (4) $\boldsymbol{M}$ represents submatrix of $\boldsymbol{G}_{\mathrm{LC1}}$ and $\boldsymbol{G}_{\mathrm{LC2}}$.

2) Power control part. This segment regulates the inverter's output power using a combination of the MPPT algorithm and DC-side voltage control mechanisms. The MPPT algorithm determines the voltage at the MPP, denoted as V_{MPP}. However, due to the MPPT's multi-second operational cycle and step-like linearization, the algorithm's detailed behavior is excluded from the analysis presented in this study. The core assumption in this segment's modeling is the instantaneous power equivalence between the AC and DC sides.

The instantaneous energy exchange in the inverter-side inductor L_{1} is considered negligible. Assuming ideal power devices with no losses, the active powers on the AC and DC sides are deemed to be instantaneously equal. The small-signal representation of the AC-side's instantaneous active power is modeled by the "Power Calc" block—presented in Fig. 2 and Eq. (5)—which supports the AC-to-DC power conversion process. To mitigate measurement noise and limit the bandwidth of the DC voltage control loop, a first-order low-pass filter is applied, thereby augmenting the stability of the dual-loop control architecture.

Assuming a negligible instantaneous energy exchange in the inverter-side inductor L_{1}, and ignoring power device losses, the active powers on the AC and DC sides are considered instantaneously equivalent—an assumption reflected in the small-signal model

by (5). As shown in Fig. 2, the "Power Calc" block is a conceptual element used to map the transformation of AC power to its DC equivalent within the model framework. To suppress measurement noise and shape the control loop bandwidth, a first-order low-pass filter is applied to the DC voltage feedback, thereby enhancing the stability of the dual-loop control system.

$$\Delta P_{\mathrm{ac}}=3/2\begin{bmatrix} I_{\mathrm{L1\_}d} & I_{\mathrm{L1\_}q} & 0 & 0 & V_{\mathrm{C1\_}d} & V_{\mathrm{C1\_}q}\end{bmatrix}\begin{bmatrix}\Delta V_{\mathrm{C1}(dq)[2\times 1]}\\ \Delta I_{\mathrm{O}(dq)[2\times 1]}\\ \Delta I_{\mathrm{L1}(dq)[2\times 1]}\end{bmatrix} \tag{5}$$

In Fig. 2, the ΔP_{ac} to ΔV_{dc} block does not exist in actual control systems. However, this study introduces it to translate variations in the AC output power, ΔP_{ac}, into corresponding changes in the DC voltage, ΔV_{dc}. This approach enables a more effective analysis of the system's behavior under various DC-side operating conditions with the PV panel. As illustrated in Fig. 3, the PV panel's output characteristics are segmented into three regions [26], [27].

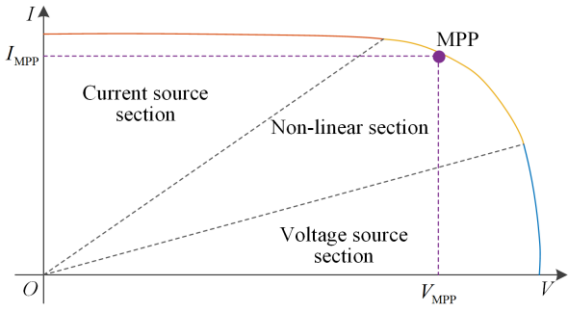

Fig. 3. Three sections of the *V*-*I* curve of PV panels.

CC section. The derivative d*I*/d*V*, representing the slope of the *I*-*V* curve, approaches zero in the CC, indicating that the current remains relatively stable, while the voltage increases gradually. A slope threshold of $\left|\mathrm{d}I/\mathrm{d}V\right|\leqslant 1$ is applied, corresponding to approximately 0.64 of the open-circuit voltage (ΔV_{oc}). In this scenario, DC-side control is inactive, and instantaneous power analysis is not required.

CV section. The voltage remains nearly stable, while the current fluctuates rapidly, causing the slope to approach negative infinity due to rapid changes in current values. This area is defined by large absolute slopes $\left|\mathrm{d}I/\mathrm{d}V\right|\geqslant 5$, corresponding approximately to $0.88V_{\mathrm{oc}}$. The small-signal expression of ΔP_{ac} with respect to ΔV_{dc} under this condition is presented in (6).

NL section. This section marks the transition between CC and CV regions. In proximity to ΔV_{MPP}, the PV panel exhibits non-linear behavior, with characteristics intermediate to those of the CV and CC sections.

$$\Delta P_{\mathrm{dc}}=-V_{\mathrm{dc}}\Delta I_{\mathrm{Cdc}}+I_{\mathrm{Odc}}\Delta V_{\mathrm{dc}}=I_{\mathrm{Odc}}\Delta V_{\mathrm{dc}}-V_{\mathrm{dc}}sC_{\mathrm{dc}}\Delta V_{\mathrm{dc}} \tag{6}$$

The proposed model also effectively analyzes scenarios in which the inverter operates in resistive rectification (RR) mode. Specifically, when the DC side is purely resistive and the AC side is supplying energy, the small-signal relationship between ΔP_{dc} and ΔV_{dc} for this condition is formulated as follows:

$$\Delta P_{\mathrm{dc}}=2\frac{V_{\mathrm{dc}}\Delta V_{\mathrm{dc}}}{R}-V_{\mathrm{dc}}sC_{\mathrm{dc}}\Delta V_{\mathrm{dc}}=2I_{\mathrm{Odc}}\Delta V_{\mathrm{dc}}-V_{\mathrm{dc}}sC_{\mathrm{dc}}\Delta V_{\mathrm{dc}} \tag{7}$$

In both CC and RR modes, the DC voltage reference from the MPPT, $\Delta V_{\mathrm{dc\_ref}}$, is compared with the current DC voltage, ΔV_{dc}, to generate the rotating *d*-axis output current reference, $\Delta I_{\mathrm{O\_}d\mathrm{ref}}$, through the DC voltage PI_1 regulator. To ensure a unit power factor, the rotating *q*-axis reference current is set to zero. In contrast, in CV mode, where DC voltage control is not applied, the active power reference is directly specified, and the output current reference is calculated using a coefficient, as follows:

$$\boldsymbol{G}_{\mathrm{CP1}[2\times 6]}=\frac{-3/2\,R_{\mathrm{PI1}}}{1+sT_{\mathrm{LP2}}}\frac{1}{k_{\mathrm{dc}}I_{\mathrm{Odc}}-sC_{\mathrm{dc}}V_{\mathrm{dc}}}\begin{bmatrix} I_{\mathrm{L1\_}d} & 0\\ I_{\mathrm{L1\_}q} & 0\\ 0 & 0\\ 0 & 0\\ V_{\mathrm{C1\_}d} & 0\\ V_{\mathrm{C1\_}q} & 0\end{bmatrix}^{\mathrm{T}},\qquad \boldsymbol{G}_{\mathrm{CP2}[2\times 1]}=-\begin{bmatrix} R_{\mathrm{PI1}}\\ 0\end{bmatrix}\Big/\begin{bmatrix}\sqrt{2}/3V_{\mathrm{C1\_}d}\\ 0\end{bmatrix} \tag{8}$$

3) Output control part. This section regulates the inverter's output current, typically using a PI regulator, PI_2, for current control on the inverter side, as shown in Fig. 2 [25]. However, the current control is dependent on the rotating frame of the feedback variables, with the rotational transformation influenced by the grid voltage and the PLL. Consequently, the effects of both the PLL and rotational transformation must be incorporated into the model [28]. By linearizing the PLL [19], [20], the transfer function, $G_{\mathrm{PLL}}(s)$, is derived, representing the relationship between the q-axis voltage and the PLL's output phase angle, as given by

$$\Delta\theta=\begin{bmatrix}0 & G_{\mathrm{PLL}}\end{bmatrix}\Delta V_{\mathrm{C1}(dq)[2\times 1]} \tag{9}$$

The small-signal relationship between the input and output of this segment is expressed in (10), where K_{PWM} denotes the PWM gain of the inverter, which scales the inverter's output control signal to the actual output voltage of the inverter bridge. When variable gain control is used, this gain becomes unitary [3]. Additionally, it incorporates delays inherent in the inverter control process, including computational, carrier loading, and carrier effectiveness delays.

$$\boldsymbol{G}_{\mathrm{CI1}[3\times6]}=K_{\mathrm{PWM}}\begin{bmatrix}0 & sG_{\mathrm{PLL}}/K_{\mathrm{PWM}} & 0&0&0&0\\ 1 & (-I_{\mathrm{L1}\_q}R_{\mathrm{PI2}}+V_{\mathrm{C1}\_q}-V_{\mathrm{inv}\_q})G_{\mathrm{PLL}} & 0&0&-R_{\mathrm{PI2}}&0\\ 0 & 1+(I_{\mathrm{L1}\_d}R_{\mathrm{PI2}}-V_{\mathrm{C1}\_d}+V_{\mathrm{inv}\_d})G_{\mathrm{PLL}} & 0&0&0&-R_{\mathrm{PI2}}\end{bmatrix},\ \boldsymbol{G}_{\mathrm{CI2}[3\times2]}=K_{\mathrm{PWM}}\begin{bmatrix}R_{\mathrm{PI2}}&0\\0&0\end{bmatrix} \tag{10}$$

C. Model in dq Domain and Positive-negative Sequence Domain

The small-signal model of the PV inverter system is developed by integrating the previously discussed three parts and resolving their input-output relationships. By combining (1), (2), and (3), a simplified expression is obtained, as follows:

$$\begin{bmatrix}\Delta V_{\mathrm{C1}(dq)[2\times1]}\\ \Delta I_{\mathrm{O}(dq)[2\times1]}\\ \Delta I_{\mathrm{L1}(dq)[2\times1]}\end{bmatrix}=\boldsymbol{T}_{\mathbf{M1}[6\times1]}\begin{bmatrix}\Delta V_{\mathrm{dcref}}\\ \Delta P_{\mathrm{cref}}\end{bmatrix}+\boldsymbol{T}_{\mathbf{M2}[6\times3]}\begin{bmatrix}\Delta\omega_{\mathrm{g}}\\ \Delta E_{\mathrm{g}(dq)[2\times1]}\end{bmatrix} \tag{11}$$

where $\boldsymbol{T}_{\mathbf{M1}}$ denotes the transfer matrix that relates the DC voltage or power reference to the inverter's state variables ($\Delta I_{\mathrm{L1}\_dq}$, $\Delta I_{\mathrm{C1}\_dq}$, and ΔI_{O_dq}), and $\boldsymbol{T}_{\mathbf{M2}}$ implies the transfer matrix that links the grid voltage and frequency to the inverter's state variables. The transfer matrices $\boldsymbol{T}_{\mathbf{M1}}$ and $\boldsymbol{T}_{\mathbf{M2}}$ are comprehensively presented in Appendix A. For instance, the conductance matrix of the inverter, representing the current-to-voltage ratio at its output, is expressed as follows:

$$\begin{bmatrix}\Delta I_{\mathrm{O}d}\\ \Delta I_{\mathrm{O}q}\end{bmatrix}=Y_{\mathrm{O}dq}\begin{bmatrix}\Delta E_{\mathrm{g}d}\\ \Delta E_{\mathrm{g}q}\end{bmatrix}=\begin{bmatrix}Y_{\mathrm{d}d}&Y_{\mathrm{d}q}\\ Y_{\mathrm{q}d}&Y_{\mathrm{q}q}\end{bmatrix}\begin{bmatrix}\Delta E_{\mathrm{g}d}\\ \Delta E_{\mathrm{g}q}\end{bmatrix}=\begin{bmatrix}\boldsymbol{T}_{\mathbf{M2}[6\times3]}(3,2)&\boldsymbol{T}_{\mathbf{M2}[6\times3]}(3,3)\\ \boldsymbol{T}_{\mathbf{M2}[6\times3]}(4,2)&\boldsymbol{T}_{\mathbf{M2}[6\times3]}(4,3)\end{bmatrix}\begin{bmatrix}\Delta E_{\mathrm{g}d}\\ \Delta E_{\mathrm{g}q}\end{bmatrix} \tag{12}$$

The indices (i, j)—following the matrix notation—represent the elements located in the ith row and jth column within the matrix. Following the approach outlined in [20], the transfer matrices in the dq domain can be converted into the positive-negative sequence domain.

III. Stability Analysis of Grid-connected System

The inverter's output impedance, crucial for the stability analysis of the grid-connected system, is derived from the model presented in Section II. The system's parameters, aligned with the simulations and experimental setups outlined in Section IV, are listed in Table I.

TABLE I
Main Hardware Parameters of PV Inverter

Symbol	Parameter	Value	Symbol	Parameter	Value
P_{n} (kVA)	Rated power	20.0	V_{o} (V)	Rated voltage	400.0
f_1 (Hz)	Grid frequency	50.0	f_{sw} (kHz)	Switching frequency	20.0
L_1 (mH)	Inv-side inductor	0.92	C_1 (μF)	Filter capacitor	3.3
L_2 (mH)	Grid-side inductor	0.06	C_2 (μF)	Filter capacitor	12.0

A. PV Inverter Operation Modes and Their Comparison

The *I-V* curve of the PV panel is divided into three distinct regions—CC, CV, and non-linear sections—described in Section II.

The output impedance of grid-connected PV inverters varies due to the fluctuations in DC-side voltages caused by the MPPT algorithm, causing it to oscillate between the impedance characteristics of the CV and CC modes. The inverter's positive and negative sequence output impedance in these modes is illustrated in Fig. 4. The actual output impedance of the PV inverter, though influenced by varying characteristics at different DC-side voltages, can be approximated by the median of the CV and CC mode impedances.

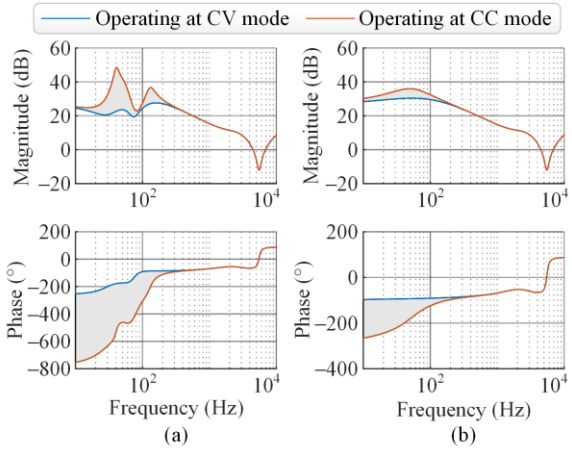

Fig. 4. Positive and negative sequence impedance of two modes. (a) Positive sequence impedance. (b) Negative sequence impedance.

A comparison of the DC-side CV and CC modes, along with the sequence impedances shown in Fig. 4, reveals the following observations:

1) Comparison of DC-side CV and CC modes. In the mid to high-frequency ranges (above 200 Hz), the inverter output impedances in the CV and CC modes are nearly identical. However, at lower frequencies (below 200 Hz), the CC mode shows a higher impedance than the CV mode, characterized by a resistive-capacitive phase characteristic.

2) Comparison of positive and negative sequence impedances. The negative sequence impedance is consistently higher and exhibits smoother frequency variation compared to the positive sequence impedance. These differences largely arise from the asymmetric control strategies of the converter—including PLL, DC-side voltage regulation, and coordinate transformations. Despite the higher magnitude of negative-sequence impedance, stability concerns, such as

oscillations, resonances, and instabilities, are frequently associated with the interaction between the inverter's positive-sequence impedance and the grid impedance. In practice, the stability margin of positive-sequence impedance is generally smaller than that of negative-sequence impedance. Consequently, stability analyses based on sequence impedance predominantly focus on examining the positive-sequence impedance [15]–[17].

B. Stability Under Different Short-circuit Ratios

An impedance-based stability criterion, as outlined in [11], is employed by partitioning the system into two subsystems: the inverter (modeled as a source) and the grid (modeled as a load). The output impedance of the inverter (Z_{inv}) and that of the grid (Z_{grid}) are computed, and their ratio (Z_{grid}/Z_{inv}) is assessed using the Nyquist stability criterion. If this ratio satisfies Nyquist's criterion—as indicated by the Nyquist plot's avoidance of encircling the origin—the inverter-grid interaction remains stable, thus preventing oscillations or instability. Alternatively, on the frequency response curve, stability can be verified by identifying intersections of the Z_{inv} and Z_{grid} amplitude curves and ensuring that their phase difference does not exceed 180°. If this condition is met, then system stability can be ensured.

Both positive and negative sequence impedances are relevant for stability analysis; however, the positive sequence component of the inverter output impedance more effectively indicates the potential system instabilities. Therefore, the stability investigation primarily focuses on the positive sequence impedance.

The output impedance of the grid-connected inverter in both CV and CC modes is compared to the grid impedance, using an open-loop magnitude-phase stability criterion. Bode plots, showing the inverter's output impedance across different modes and grid impedance for various SCRs, are shown in Fig. 5.

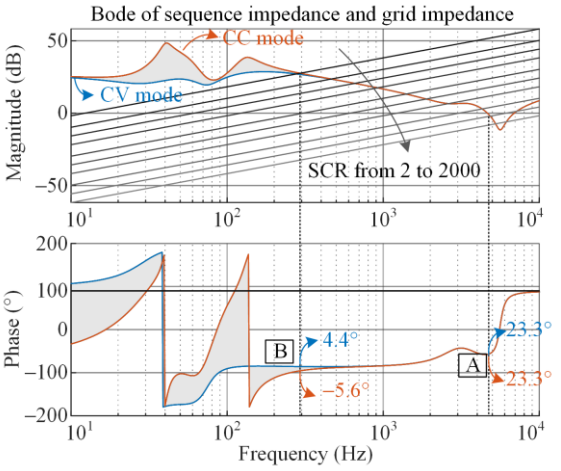

Fig. 5. Bode of sequence impedance and grid impedance.

The grid impedance values are SCRs ranging from 2 to 2000, with SCR equaling 2000 chosen to simulate an approximately ideal strong grid condition. This selection enables a more effective analysis of the inverter's stability evolution characteristics. Achieving such a high SCR value is uncommon in practical power systems. The phase margin is determined by the phase difference at the intersection point where the inverter output impedance amplitude intersects with the grid impedance amplitude.

The analysis reveals the following observation:

1) At high SCRs: The grid impedance is minimal, reducing the system's stability margin in both CV and CC modes. The phase margin at point A in Fig. 8 is approximately 23.3° at around 5000 Hz, which may trigger resonance and threaten system stability.

2) As the SCR diminishes: The grid impedance escalates, which initially enhances the stability margin, before causing a sharp decline. When the SCR reaches 3, the phase margin approaches 0, signaling the stability threshold.

3) At low SCRs: The low-frequency output impedance is contrasted between CV and CC modes. In the SCR range of 2–5, the phase margin in CV mode remains below 5°, while it becomes negative in the CC mode at point B. Within this range, the CV mode demonstrates greater stability than the CC mode.

C. Stability with Different Regulators' Gain

The output impedance of the inverter, considering variations in the DC voltage and AC current loop regulators, is derived from the established model. The influence of these parameters on the inverter's output impedance and system stability is then analyzed. The design of the DC voltage loop and AC current loop regulator parameters follows the methodologies outlined in [14], [29], and [30].

Variations in the proportional gain of the DC voltage loop, $R_{PI1} \cdot K_p$, from 0.5 p.u. to 2.0 p.u., affect the inverter's output impedance characteristics, as shown in Fig. 6.

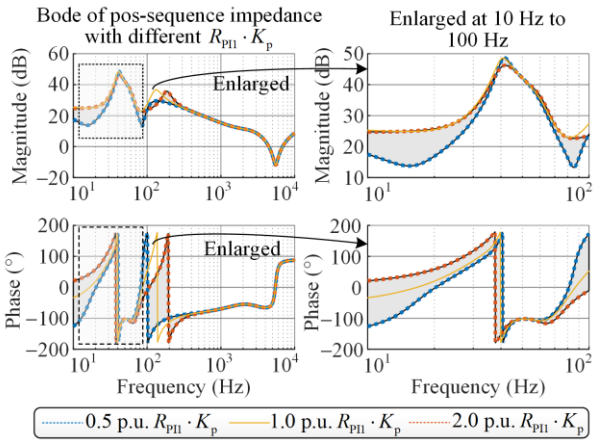

Fig. 6. Bode of sequence impedance with different R_{PI1} parameters.

The $R_{PI1} \cdot K_p$ primarily influences the low-frequency band (below 200 Hz), with minimal impact on the mid- and high-frequency bands (above 200 Hz). An increase in $R_{PI1} \cdot K_p$ leads to a higher inverter output impedance amplitude and a decrease in phase within this range.

Conversely, variations in the proportional term of the AC current loop regulator, $R_{PI2} \cdot K_p$, ranging from 0.5 p.u. to 4.0 p.u., affect the inverter output impedance at mid- and high-frequency bands (above 200 Hz), as illustrated in Fig. 7.

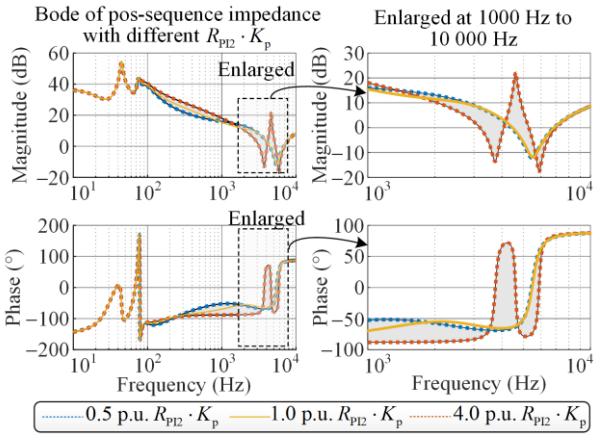

Fig. 7. Bode of sequence impedance with different R_{PI2} parameters.

The $R_{PI2} \cdot K_p$ influences the mid-frequency range (200–1000 Hz), where an increase in $R_{PI2} \cdot K_p$ results in higher impedance and a reduced phase. In the high-frequency range, a higher $R_{PI2} \cdot K_p$ can cause complex variations in the inverter output impedance.

The system's stability across various SCRs and regulator parameters is analyzed to establish a theoretical foundation for enhancing the stability of inverter operation in environments with high renewable penetration.

The minimum phase stability margins and corresponding frequencies at various SCRs (2–2000 Hz) are shown in Fig. 8 (a) and 8(c) for $R_{PI1} \cdot K_p$ values range between 0.5 p.u. and 2.0 p.u. Similarly, Fig. 8(b) and (d) shows the minimum phase stability margins and their frequencies for $R_{PI2} \cdot K_p$ values ranging from 0.5 p.u. to 4.0 p.u. This analysis indicates the following observations:

1) Minimum phase margin: As the SCR decreases, the overall phase margin of the system demonstrates a declining decrease, though the stability margin registers an increase within mid- to high-frequency bands. The system attains critical stability at an SCR of 5.

2) Frequency points of minimum phase margin: Similar to the phase margin, the frequency corresponding to the minimum phase margin generally decreases as SCR decreases, except for an increase observed within a specific frequency band.

3) DC voltage regulator PI_1: The $R_{PI1} \cdot K_p$ parameter has a minimal impact on system stability when large SCRs are used. However, its effect becomes more significant with smaller SCRs, particularly near critical stability thresholds, where a higher $R_{PI1} \cdot K_p$ diminishes the system's stability margin and worsens instability.

4) AC current regulator PI_2: Unlike PI_1, a smaller SCR diminishes the impact of $R_{PI2} \cdot K_p$ on system stability, though an increase in $R_{PI2} \cdot K_p$ may decrease the stability margin. At higher SCRs, the $R_{PI2} \cdot K_p$ significantly affects system stability, leading to complex behavior. While a larger $R_{PI2} \cdot K_p$ can improve the stability margin within certain SCR ranges, it may reduce it in others. Nonetheless, an excessively high $R_{PI2} \cdot K_p$ could trigger harmonic resonance near the LCL filter's cut-off frequency, particularly in the mid-frequency range.

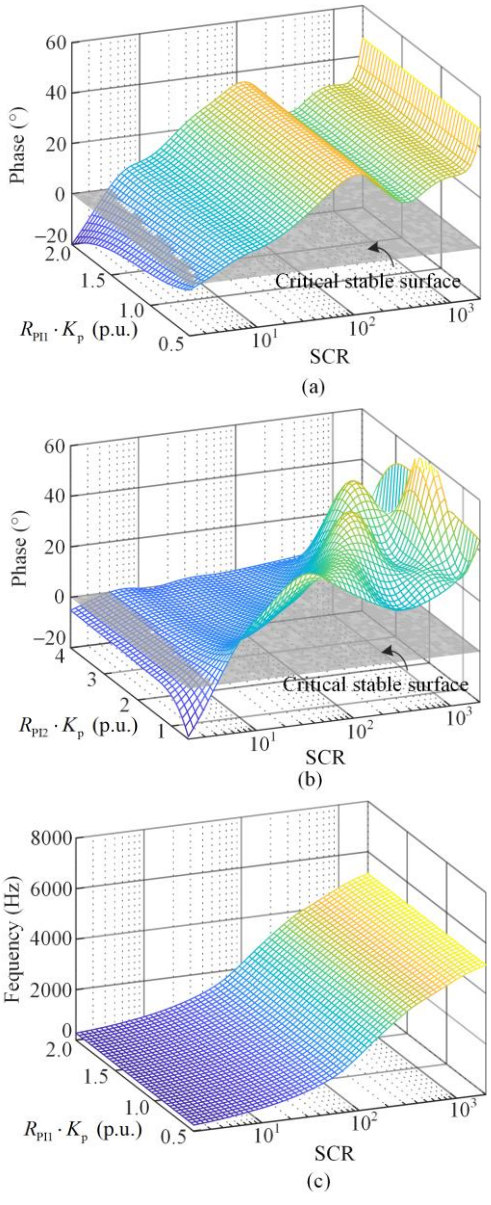

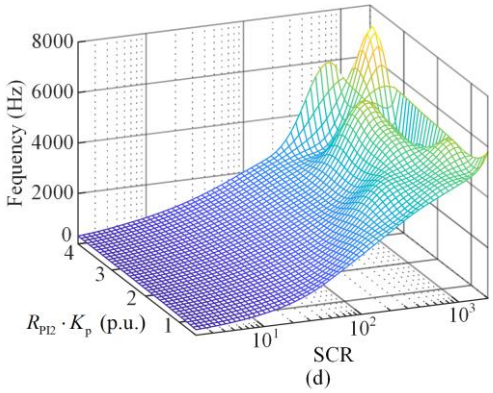

Fig. 8. Surface of minimum phase stability margin and their frequency. (a) The phase stability margin with $R_{PI1} \cdot K_p$ varies. (b) The phase stability margin with $R_{PI2} \cdot K_p$ varies. (c)The corresponding frequencies with $R_{PI1} \cdot K_p$ varies. (d) The corresponding frequencies with $R_{PI2} \cdot K_p$ varies.

IV. Guidelines for Graphics Preparation and Submission

A. Simulation and Experimental Platform

The simulation and experimental apparatus comprise a 20-kW T-type LCL transformerless PV inverter, featuring a variable inductance configuration, as shown in Fig. 9. An autonomous DC source supplies the DC energy, which the inverter converts into AC. This AC output is transmitted through a multi-scale variable inductance designed to simulate various grid impedances. The assemblage's culmination is then connected to a grid simulator, ensuring the maintenance of an ideal grid voltage. The primary hardware components and their rated parameters are listed in Table I.

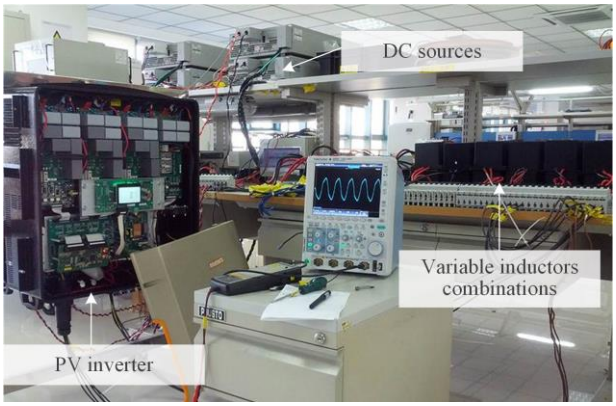

Fig. 9. Experimental platform.

B. Simulation- Frequency Sweep of Output Impedance

As shown in Figs. 10(a)–(c), the frequency-dependent output impedance of the PV inverter is depicted under three different DC-side operating modes: CV, CC, and RR, respectively. These modes are assessed under full load and one-third load conditions. The solid lines depict the amplitude-phase curves predicted by the model developed in this study, whereas the dotted lines represent the amplitude-phase points obtained from frequency sweep simulations.

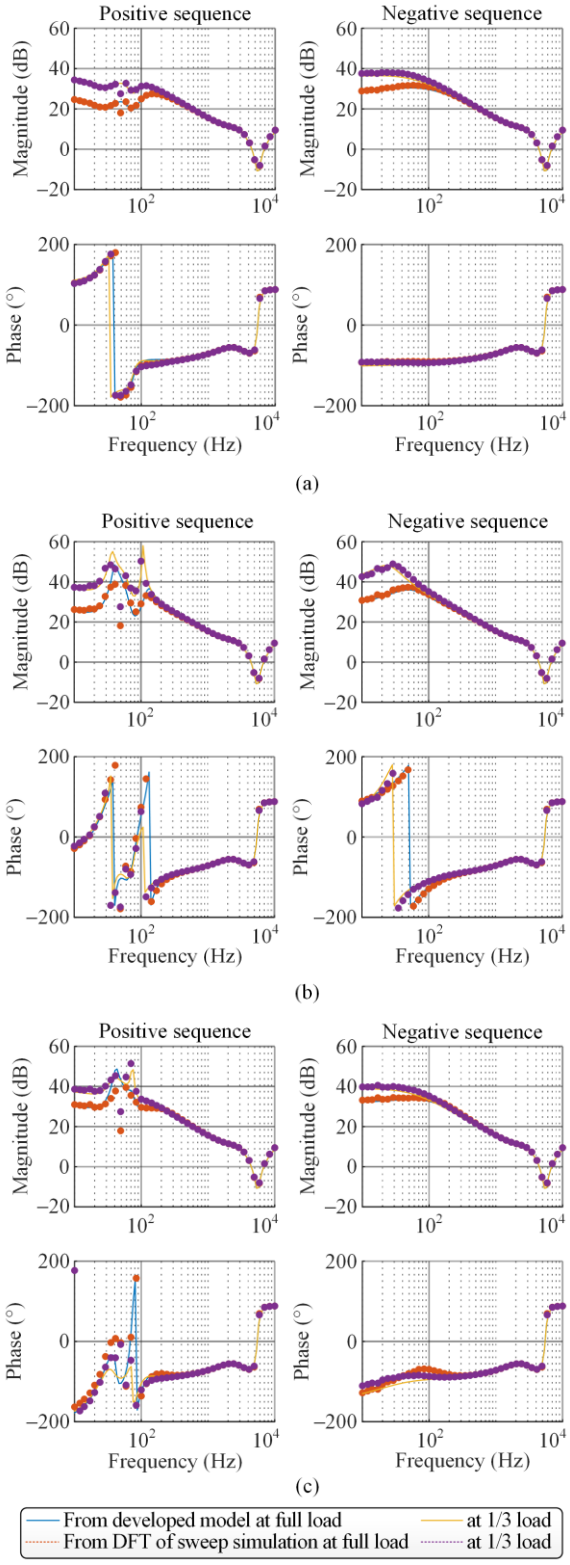

Fig. 10. Inverter output impedance curves for the DC side at different operating modes. (a) CV operation mode. (b) CC operation mode. (c) RR operation mode.

1) The modeled and simulated frequency responses show congruence from 10 Hz up to 10 kHz.

2) A deviation at 50 Hz is observed, primarily due to the influence of the grid's fundamental voltage and current components.

3) Discrepancies below 100 Hz occur in CC and RR modes on the DC side, resulting from the modeling assumption of equal instantaneous power on the AC and DC sides and the omission of the instantaneous power of the AC inductors.

4) The variations in PV panel irradiance influence the output power of the grid-connected inverter, with higher irradiance yielding greater output power. The output power fluctuations primarily affect the impedance characteristics of the grid-connected inverter in the low-frequency range (＜100 Hz), where higher irradiance and output power correspond to reduced output impedance.

These simulations substantiate the modeling approach outlined in Section II.

C. Experimental-Stability Under Different SCRs

This section validates the analysis from Section III.B by simulating various grid impedances using several inductor configurations connected in series and parallel.

First, the simulation considers a scenario where the grid SCR decreases progressively from 20 to 2.5, as illustrated in Fig. 11(a). The grid SCR transitions sequentially through values of 20, 10, 5, and 2.5, showing the corresponding inverter output current at each stage (Figs. 11(b)–(e)). The FFT analysis of the output current for each stage is shown in Fig. 11(f). From Fig. 11, the following observations can be drawn:

1) In the time-domain waveforms, the inverter output current remains smooth and stable when the SCR is 20, 10, and 5 (Figs. 11(a)–(c)). However, at an SCR of 2.5 (Fig. 11(e)), the inverter output current waveform exhibits significant distortion.

2) In the frequency-domain waveform shown in Fig. 11(f), as SCR decreases, harmonic frequencies progressively diminish, accompanied by a slight increase in their amplitudes. When SCR reaches 2.5, a sharp rise in harmonic amplitude is observed around 350 Hz.

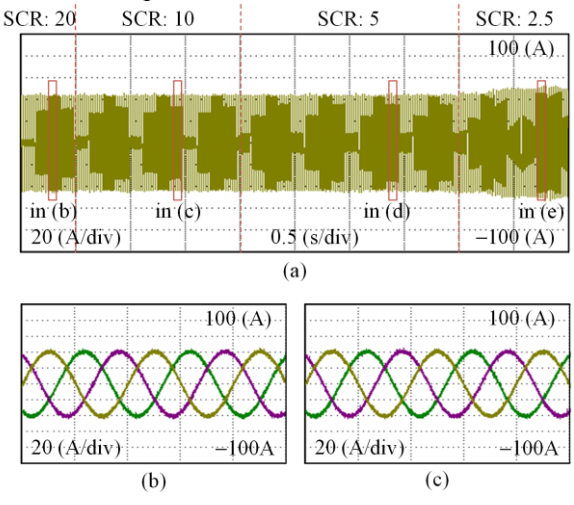

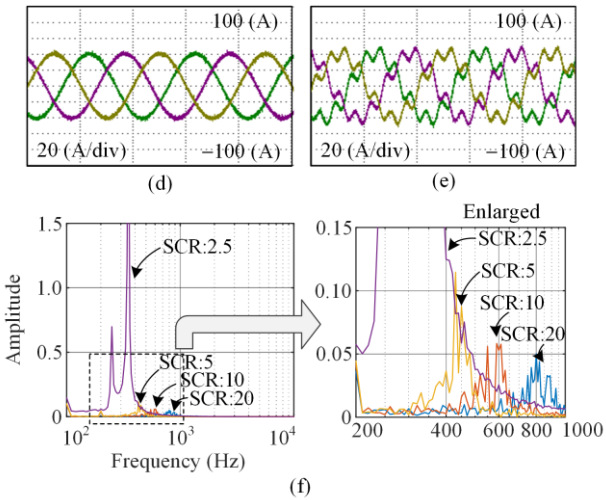

Fig. 11. Inverter output current and their FFT under different SCRs (from 20 to 2.5). (a) Inverter output current with the grid SCR decreases progressively from 20 to 2.5. (b) SCR equals 20. (c) SCR equals 10. (d) SCR equals 5. (e) SCR equals 2.5. (f) FFT of inverter output current under different SCRs.

Next, a simulation is conducted in which the grid SCR increases progressively from 20 to 1000, as depicted in Fig. 12(a). The grid SCR transitions sequentially through the values 20, 100, 500, and 1000, showing the corresponding inverter output current at each stage (Fig. 12(b)–(e)), respectively. The FFT analysis of the output current at each stage is presented in Fig. 12(f). From Fig. 12, it can be observed that:

1) In the time-domain waveforms, the inverter output current remains smooth and stable when the SCR equals 20, 100, and 500 (Fig. 12(a)–(c)). However, at an SCR value of 1000 (Fig. 12(e)), the output current waveform exhibits considerable resonance.

2) In the frequency-domain waveform shown in Fig. 12(f), as SCR increases, harmonic frequencies rise gradually, with their amplitudes first decreasing and then increasing. When SCR equals 1000, a sharp increase in harmonic amplitude occurs at approximately 4500 Hz.

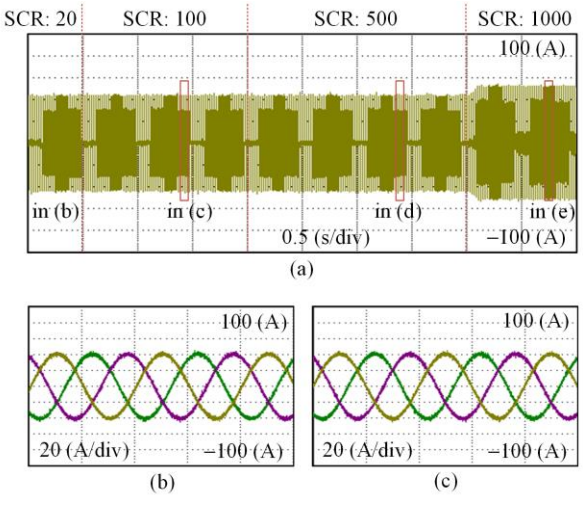

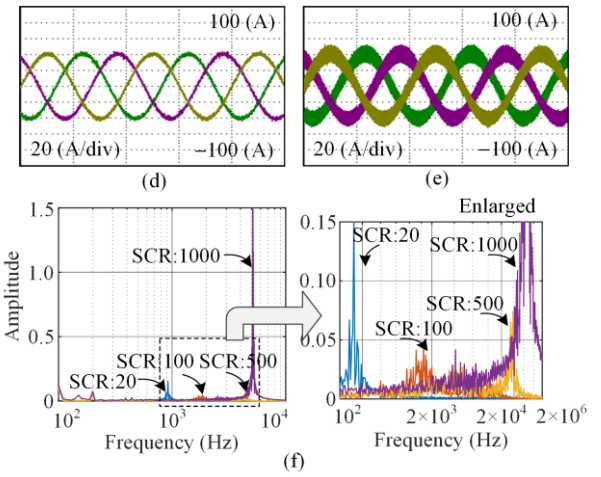

Fig. 12. Inverter output current and their FFT under different SCRs (from 20 to 1000). (a) Inverter output current with the grid SCR increases progressively from 20 to 1000. (b) SCR equals 20. (c) SCR equals 100. (d) SCR equals 500. (e) SCR equals 1000. (f) FFT of inverter output current under different SCRs.

The characteristics observed at SCR values of 40, 60, and 80 exhibit patterns similar to those observed at SCR equaling 20 and SCR equaling 100 cases. As a result, their corresponding waveforms are not presented and analyzed in Fig. 12.

These findings validate the analysis presented in Section III.B.

D. Experimental-Stability Comparison of CV and CC

An additional analysis of the stability of the DC-side of a PV grid-connected inverter operating in CV, MPPT, and CC modes is conducted. The effects of varying irradiance levels on the stability of the grid-connected inverter are verified, as detailed in Section III.B.

During steady-state operation of the grid-connected inverter, the SCR is switched from 20 to 3. Figure 13 illustrates the output current waveform of the grid-connected inverter. Figures 13(a)–(c) show the output current waveforms when the inverter operates at full power under an irradiance level of 1000 W/m^2 in CV, MPPT, and CC modes. Figure 13(d) presents the fast Fourier transform (FFT) results for Figs. 13(a)–(c) after the SCR is set to 3 during steady-state operation. The right side of Figs. 13(e)–(g) shows the output current waveforms when the inverter operates at half power under an irradiance level of 500 W/m^2 in CV, MPPT, and CC modes. Figure 13(h) depicts the FFT results for Figs. 13(e)–(g) after the SCR is switched to 3 during steady-state operation.

The following observations are made:

1) In CV mode, a transient distortion appears in the inverter's output current waveform when the grid's SCR decreases from 20 to 3, as shown in Fig. 13(a). The output current stabilizes after approximately one cycle, returning to its normal state. In contrast, under MPPT and CC modes, a similar decrease in SCR from 20 to 3 causes substantial distortion in the inverter's output current waveform—which persists into steady-state operation—as shown in Figs. 13(b) and (c). This observation indicates that, under weak grid conditions, the stability of a grid-connected inverter is reduced in CC and MPPT modes compared to that in CV mode.

2) When the irradiance is reduced from 1000 W/m^2 (full power) to 500 W/m^2 (half power), a similar trend is observed. As the grid SCR decreases from 20 to 3, the stability of the inverter operating in CC and MPPT modes becomes inferior compared to its performance in CV mode (Figs. 13(e)–(g)). This observation suggests that under weak grid conditions, variations in irradiance (output power) have a minimal impact on inverter stability.

3) Steady-state FFT analysis of the output current at SCR equaling 3 under irradiances of 1000 W/m^2 and 500 W/m^2 indicates significant harmonic amplification around 400 Hz in both CC and MPPT modes, with higher harmonic amplitude observed in the CC mode. In contrast, the harmonic amplification in this frequency range is minimal in the CV mode.

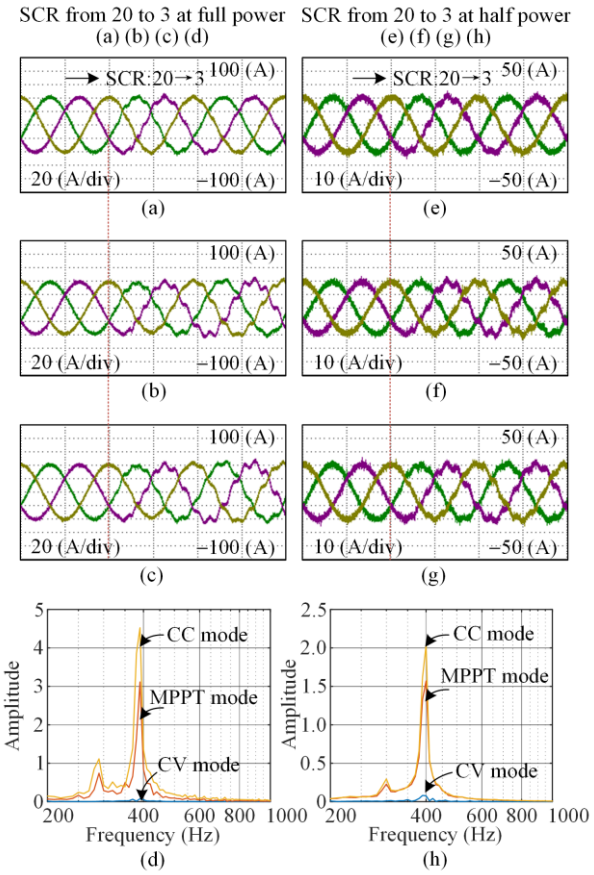

Fig. 13. Inverter output current and their FFT under CC and CV modes. (a) Inverter output current at CV mode. (b) Inverter output current at MPPT mode. (c) Inverter output current at CC mode. (d) FFT of inverter output current in (a)–(c) after SCR set to 3. (e) Inverter output current at CV mode under half power. (f) Inverter output current at MPPT mode under half power. (g) Inverter output current at CC mode under half power. (h) FFT of inverter output current in (e)–(g) after SCR set to 3.

Therefore, these results confirm that a grid-connected inverter operating in the CV mode offers the highest stability under weak grid conditions, while the CC mode exhibits the lowest stability. The MPPT mode demonstrates intermediate stability, falling between these two modes. These findings corroborate the analysis presented in Section III.B of this study. Additionally, although irradiance influences the inverter's output power, its effect on stability under weak grid conditions is negligible.

E. Experimental-Influence of Regulators' Gain

The final experiment evaluates the impact of regulator parameter variations on the stability of the grid-connected inverter, as described in Sections III.C and D of this study. Specifically, the proportional gains $R_{\mathrm{PI1}} \cdot K_{\mathrm{p}}$ and $R_{\mathrm{PI2}} \cdot K_{\mathrm{p}}$ associated with the DC voltage and AC current loop regulators were systematically adjusted to examine their influence on the output current and its FFT. Our analysis identified two critical points of instability occurring at SCR values of 4 and 1000. The parameter adjustments for the regulators are presented in Table II.

TABLE II
PI1 AND PI2 REGULATORS' PARAMETERS

Figure 13	$R_{\mathrm{PI1}} \cdot K_{\mathrm{p}}$ and $R_{\mathrm{PI2}} \cdot K_{\mathrm{p}}$ (p.u.)			SCR
	Stage I	Stage II	Stage III	
(a), (e)	1.0 / 1.0	1.5 / 1.0	2.0 / 1.0	4
(b), (f)	1.0 / 1.0	1.5 / 1.0	2.0 / 1.0	1000
(c), (g)	1.0 / 1.0	1.0 / 2.0	1.0 / 2.5	4
(d), (h)	1.0 / 1.0	1.0 / 2.0	1.0 / 2.5	1000

The inverter operates in the CC mode, and the results are presented in Fig. 14. Specifically, Figs. 14(a), (b), (e), and (f) shows the influence of the PI_1 regulator gain on system stability, where $R_{\mathrm{PI1}} \cdot K_{\mathrm{p}}$ is varied from 1.0 to 2.0 p.u. and then to 2.5 p.u., under SCR conditions of 4 and 1000. Similarly, Figs. 14(c), (d), (g), and (h) illustrates the effect of varying PI_2 regulator gain on system stability, with $R_{\mathrm{PI2}} \cdot K_{\mathrm{p}}$ varied across the same range under identical SCR conditions. These analyses evaluate how regulator gain adjustments influence system stability across different SCR scenarios, leading to the following conclusions:

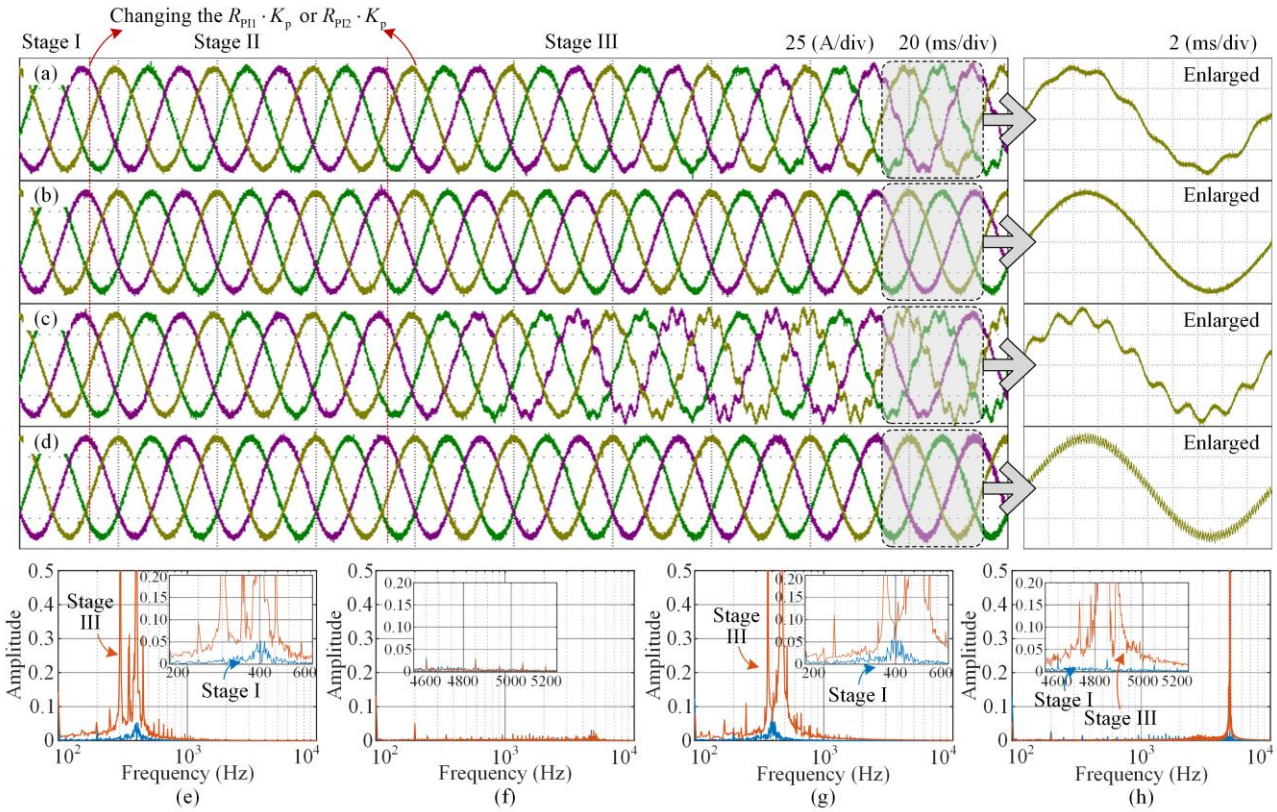

Fig. 14. Inverter output currents and their FFT with PI regulators changes: (a) Inverter output current with $R_{\mathrm{PI1}} \cdot K_{\mathrm{p}}$ varies and SCR equals 4. (b) Inverter output current with $R_{\mathrm{PI1}} \cdot K_{\mathrm{p}}$ varies and SCR equals 1000. (c) Inverter output current with $R_{\mathrm{PI1}} \cdot K_{\mathrm{p}}$ varies and SCR equals 4. (d) Inverter output current with $R_{\mathrm{PI1}} \cdot K_{\mathrm{p}}$ varies and SCR equals 1000. (e) FFT of inverter output current in (a). (f) FFT of inverter output current in (b). (g) FFT of inverter output current in (c). (h) FFT of inverter output current in (d).

1) At an SCR value of 4, increasing $R_{\mathrm{PI1}} \cdot K_{\mathrm{p}}$ from 1.0 to 2.0 p.u. and subsequently to 2.5 p.u. causes significant distortions in the output current. A similar effect isobserved when $R_{\mathrm{PI2}} \cdot K_{\mathrm{p}}$ is increased from 1.0 to 2.0 p.u.

and then to 2.5 p.u., yielding comparable output current distortion. The FFT analysis, as shown in Figs. 14(e) and (f), indicates that this distortion primarily arises from the amplification of low-frequency harmonics, with a dominant contribution centered around the 7th harmonic component.

At an SCR value of 1000, increasing $R_{\mathrm{PI1}} \cdot K_{\mathrm{p}}$ from 1.0 to 2.0 p.u. and subsequently to 2.5 p.u. does not result in any notable changes to the output current. In contrast, a similar increase in $R_{\mathrm{PI2}} \cdot K_{\mathrm{p}}$ introduces high-frequency components into the output waveform. FFT analysis, as shown in Figs. 14(g) and (h), reveals that these components are high-frequency harmonics, predominantly concentrated near 5000 Hz, which is close to the LCL filter's cutoff frequency.

The experimental results validate the findings presented in Sections III.C and III.D of this study. The inverter's low-frequency stability is affected by both $R_{\mathrm{PI1}} \cdot K_{\mathrm{p}}$ (the proportional term of the DC voltage loop regulator) and $R_{\mathrm{PI2}} \cdot K_{\mathrm{p}}$ (the proportional term of the AC current loop regulator). Excessive values for either $R_{\mathrm{PI1}} \cdot K_{\mathrm{p}}$ or $R_{\mathrm{PI2}} \cdot K_{\mathrm{p}}$ will cause an amplification of low-frequency harmonics in the output current. Meanwhile, the stability of mid- and high-frequency components is predominantly influenced by $R_{\mathrm{PI2}} \cdot K_{\mathrm{p}}$. An excessively large value for this parameter can induce harmonic resonance at mid-frequencies and high frequencies within the output current.

V. Conclusion

This study examines the development of a small-signal model for a single-stage PV grid-connected inverter, with the primary focus on incorporating DC-side voltage control into the proposed model. This approach accounts for the various operating modes on the DC side that result from the PV panel characteristics. This study further analyzes the effects of SCR, DC-side operating mode, and variations in regulator parameters on system stability. Finally, a 20-kW PV inverter experimental and simulation platform was developed to validate the model and analyze system characteristics, yielding the following conclusions:

1) This study develops a single-stage inverter model that incorporates both DC-side characteristics and voltage control. The model has been validated through simulations and experiments. However, some instantaneous reactive power related to AC inductance was omitted during modeling, causing minor deviations at frequencies below 50 Hz. This deviation does not significantly impact stability analysis for grid-connected inverters.

2) The stability of PV grid-connected systems is significantly influenced by the SCR at the point of connection. Higher SCR values typically lead to the occurrence of medium- or high-frequency harmonic resonances in inverter output currents. However, lower SCR values can intensify the amplification of low-frequency harmonics.

3) An inverter's DC-side control can function under different modes based on the characteristics of the PV array: CV, CC, and MPPT modes, which operate between these two modes. Among these modes, the CC mode tends to exhibit lower stability than the CV mode, especially under weak grid conditions with low SCR values. Therefore, in weak grids where low-frequency harmonic amplification or proximity to stability boundaries is detected in the output current, increasing the DC-side voltage to enter the CV mode can improve system stability. Lowering the voltage may reduce the output power; however, it does not improve system stability.

4) The PI regulator in the DC voltage loop primarily governs the inverter's low-frequency dynamic characteristics, while the PI regulator in the AC current control loop predominantly affects its mid- to high-frequency characteristics. An increase in the DC-side voltage regulator gain tends to compromise system stability under low-SCR conditions. Similarly, raising the gain of the AC current regulators diminishes system stability across both low- and high-SCR conditions. Consequently, under weak grid conditions, indicators such as low-frequency harmonic amplification or proximity to stability margins in the output current suggest potential instability. In response, simultaneously reducing the gains of both the DC-side voltage and AC-side current regulators can effectively enhance overall system stability.

In conclusion, this study offers a detailed examination of the dynamic behavior of single-stage grid-connected PV inverters, offering a solid theoretical basis for enhancing their operational stability under weak grid scenarios. While the findings present a meaningful step toward improved inverter performance, the analysis is confined to single-stage PV grid-connected inverters. To build upon this foundation, further research is needed for modeling and analyzing the stability of two-stage inverters. Additionally, developing targeted solutions to improve stability under weak grids—particularly through adaptive schemes—will be the central focus of future research.

Appendix A

The detailed expressions of M_1—M_{12} in (4).

$$\boldsymbol{M}_{1[2\times1]} = -\boldsymbol{M}_{\mathrm{den}[2\times2]}^{-1}\begin{pmatrix}\boldsymbol{A}_{3[2\times2]}\boldsymbol{W}_{\mathrm{i1}[2\times1]} - \boldsymbol{A}_{1[2\times2]}\boldsymbol{W}_{\mathrm{i3}[2\times1]} + \\ \boldsymbol{A}_{1[2\times2]}\boldsymbol{A}_{3[2\times2]}\boldsymbol{W}_{\mathrm{i2}[2\times1]}\end{pmatrix} \tag{A1}$$

$$\boldsymbol{M}_{5[2\times1]} = -\boldsymbol{M}_{\mathrm{den}[2\times2]}^{-1}\begin{pmatrix}\boldsymbol{W}_{\mathrm{i1}[2\times1]} + \boldsymbol{W}_{\mathrm{i3}[2\times1]} + \boldsymbol{A}_{1[2\times2]}\boldsymbol{W}_{\mathrm{i2}[2\times1]} + \\ \boldsymbol{A}_{1[2\times2]}\boldsymbol{A}_{2[2\times2]}\boldsymbol{W}_{\mathrm{i3}[2\times1]}\end{pmatrix} \tag{A2}$$

$$\boldsymbol{M}_{9[2\times1]}=-\boldsymbol{M}_{\mathrm{den}[2\times2]}^{-1}\begin{pmatrix}\boldsymbol{W}_{\mathrm{i}1[2\times1]}+\boldsymbol{W}_{\mathrm{i}3[2\times1]}-\boldsymbol{A}_{3[2\times2]}\boldsymbol{W}_{\mathrm{i}2[2\times1]}+\\ \boldsymbol{A}_{2[2\times2]}\boldsymbol{A}_{3[2\times2]}\boldsymbol{W}_{\mathrm{i}1[2\times1]}\end{pmatrix} \quad (A3)$$

$$\boldsymbol{M}_{3[2\times1]}=-\boldsymbol{M}_{\mathrm{den}[2\times2]}^{-1}\begin{pmatrix}\boldsymbol{A}_{3[2\times2]}\boldsymbol{W}_{\mathrm{g}1[2\times1]}-\boldsymbol{A}_{1[2\times2]}\boldsymbol{W}_{\mathrm{g}3[2\times1]}+\\ \boldsymbol{A}_{1[2\times2]}\boldsymbol{A}_{3[2\times2]}\boldsymbol{W}_{\mathrm{g}2[2\times1]}\end{pmatrix} \quad (A4)$$

$$\boldsymbol{M}_{8[2\times1]}=-\boldsymbol{M}_{\mathrm{den}[2\times2]}^{-1}\begin{pmatrix}\boldsymbol{W}_{\mathrm{g}1[2\times1]}+\boldsymbol{W}_{\mathrm{g}3[2\times1]}+\\ \boldsymbol{A}_{1[2\times2]}\boldsymbol{W}_{\mathrm{g}2[2\times1]}+\\ \boldsymbol{A}_{1[2\times2]}\boldsymbol{A}_{2[2\times2]}\boldsymbol{W}_{\mathrm{g}3[2\times1]}\end{pmatrix} \quad (A5)$$

$$\boldsymbol{M}_{11[2\times1]}=-\boldsymbol{M}_{\mathrm{den}[2\times2]}^{-1}\begin{pmatrix}\boldsymbol{W}_{\mathrm{g}1[2\times1]}+\boldsymbol{W}_{\mathrm{g}3[2\times1]}-\\ \boldsymbol{A}_{3[2\times2]}\boldsymbol{W}_{\mathrm{g}2[2\times1]}+\\ \boldsymbol{A}_{2[2\times2]}\boldsymbol{A}_{3[2\times2]}\boldsymbol{W}_{\mathrm{g}1[2\times1]}\end{pmatrix} \quad (A6)$$

$$\boldsymbol{M}_{2[2\times2]}=\boldsymbol{M}_{\mathrm{den}[2\times2]}^{-1}\times\boldsymbol{A}_{3[2\times2]},\ \boldsymbol{M}_{6[2\times2]}=\boldsymbol{M}_{\mathrm{den}[2\times2]}^{-1}\times I_{[2\times2]} \quad (A7)$$

$$\boldsymbol{M}_{4[2\times2]}=\boldsymbol{M}_{\mathrm{den}[2\times2]}^{-1}\boldsymbol{A}_{1[2\times2]} \quad (A8)$$

$$\boldsymbol{M}_{8[2\times2]}=\boldsymbol{M}_{\mathrm{den}[2\times2]}^{-1}\left(\boldsymbol{A}_{1[2\times2]}\boldsymbol{A}_{2[2\times2]}+I_{[2\times2]}\right) \quad (A9)$$

$$\boldsymbol{M}_{10[2\times2]}=\boldsymbol{M}_{\mathrm{den}[2\times2]}^{-1}\left(\boldsymbol{A}_{2[2\times2]}\boldsymbol{A}_{3[2\times2]}+I_{[2\times2]}\right) \quad (A10)$$

$$\boldsymbol{M}_{12[2\times2]}=-\boldsymbol{M}_{\mathrm{den}[2\times2]}^{-1}I_{[2\times2]} \quad (A11)$$

$$\boldsymbol{M}_{\mathrm{den}[2\times2]}=\boldsymbol{A}_{1[2\times2]}+\boldsymbol{A}_{3[2\times2]}+\boldsymbol{A}_{1[2\times2]}\boldsymbol{A}_{2[2\times2]}\boldsymbol{A}_{3[2\times2]} \quad (A12)$$

The detail expressions of T_{M1} and T_{M2} in (11).

$$\boldsymbol{T}_{\mathrm{M1}}=\left[I-\boldsymbol{G}_{\mathrm{LC1}[6\times3]}\left(\boldsymbol{G}_{\mathrm{VI1}[3\times6]}+\boldsymbol{G}_{\mathrm{VI2}[3\times2]}\boldsymbol{G}_{\mathrm{VP1}[2\times6]}\right)\right]^{-1}\times \boldsymbol{G}_{\mathrm{LC1}[6\times3]}\boldsymbol{G}_{\mathrm{VI2}[3\times2]}\boldsymbol{G}_{\mathrm{VP2}[2\times2]} \quad (A13)$$

$$\boldsymbol{T}_{\mathrm{M2}}=\left[I-\boldsymbol{G}_{\mathrm{LC1}[6\times3]}\left(\boldsymbol{G}_{\mathrm{VI1}[3\times6]}+\boldsymbol{G}_{\mathrm{VI2}[3\times2]}\boldsymbol{G}_{\mathrm{VP1}[2\times6]}\right)\right]^{-1}\times \boldsymbol{G}_{\mathrm{LC2}[6\times3]} \quad (A14)$$

AUTHORS' CONTRIBUTIONS

Haizhen Xu: conceptualization and methodology. Changzhou Yu: writing-original draft preparation, visualization and conceptualization. Chen Chen: writing-review and editing. Leilei Guo: formal analysis. Jianming Su: resources. Ming Li: methodology. Xing Zhang: supervision. All authors read and approved the final manuscript.

FUNDING

This work is supported in part by the Youth Project of National Natural Science Foundation of China (No. 51907046), the University Natural Sciences Research Project of Anhui Province Project (No. 2022AH030154), and the University Synergy Innovation Program of Anhui Province (No. GXXT-2022-021).

DECLARATIONS

Competing interests: The authors declare that they have no known competing financial interests or personal relationships that could have appeared to influence the work reported in this article.

AUTHORS' INFORMATION

Haizhen Xu was born in Anhui, China, in 1988. She received the B.S. and Ph.D. degrees in electrical engineering and automation from Hefei University of Technology, Hefei, China, in 2010 and 2017. She is currently an associate professor in electrical engineering with Hefei University. Her current research interests include control of VSG converters and renewable energy generation technologies.

Changzhou Yu was born in Sichuan, China, in 1987. He received the B.S. and Ph.D. degrees in electrical engineering and automation from Hefei University of Technology, Hefei, China, in 2009 and 2016. He is currently a professor in Electrical Engineering with Hefei University. His current research interests include advanced inverter control, multi-inverter parallel system analysis and enhancement and hybrid system analysis.

Chen Chen was born in Anhui, China, in 1984. She received the B.S. degree in biotechnology from Anhui University, Hefei, China, in 2006 and the M.S. degree in kinesiology from East China Normal University, Shanghai, China, in 2010. Since 2014, she has been a faculty member of the School of Advanced Manufacturing Engineering, Hefei University. Her current research interests include new energy and environment and bioelectronics.

Leilei Guo was born in Henan, China, in 1987. He received the B.S. and the Ph.D. degree in electrical engineering from the School of Electrical Engineering and Automation, Hefei University of Technology, Hefei, China, in 2010 and 2016, respectively. He is currently an associate professor in electrical engineering with Zhengzhou University of Light Industry. He was selected into the young talent promotion plan of Henan province in 2018. His current research interests include model predictive control of motors, and power converters.

Jianming Su was born in 1987 in Anhui, China. He received his bachelor's and master's degrees in electrical engineering and automation from Hefei University of Technology, China in 2009 and 2012. He is currently a senior engineer at State Grid Tongling

Power Supply Company. He is currently engaged in power quality technology.

Ming Li was born in Anhui, China, in 1993. He received the B.S. degree in electric engineering and automation and the Ph.D. degree in electric engineering from the Hefei University of Technology, Hefei, China, in 2014 and 2020, respectively. His current research interests include control of photovoltaic converters, microgrid systems, distributed generation systems, and stability analysis of grid-connected inverters.

Xing Zhang was born in Shanghai, China, in 1963. He received the B.S., M.S., and Ph.D. degrees in electrical engineering and automation from Hefei University of Technology, Hefei, China, in 1984, 1990, and 2003, respectively. Since 1984, he has been a faculty member in the School of Electric Engineering and Automation, Hefei University of Technology, where he is currently a professor. He is also with the Photovoltaic Engineering Research Center of the Ministry of Education. His main research interests include photovoltaic generation technologies, wind power generation technologies, and distributed generation systems.

REFERENCES

[1] Pourasl, H. Hamed, and Reza Vatankhah Barenji *et al*., "Solar energy status in the world: a comprehensive review," *Energy Reports*, vol. 10, pp. 3474-3493, Jan. 2023.

[2] H. Xu, W. Wang, and C. Yu *et al*., "An improved virtual capacitor algorithm for reactive power sharing in multi-paralleled distributed generators," *IEEE Transactions on Power Electronics*, vol. 34, no. 11, pp. 10786-10795, Nov. 2019.

[3] C. Yu, X. Zhang, and F. Liu *et al*., "Modeling and resonance analysis of multiparallel inverters system under asynchronous carriers conditions," *IEEE Transactions on Power Electronics*, vol. 32, no. 4 pp. 3192-3205, Apr. 2016.

[4] B. Hu, L. Zhan, and S. Sahoo *et al*., "Synchronization stability analysis under ultra-weak grid considering reactive current dynamics," *IEEE Transactions on Industrial Electronics*, vol. 71, no. 11, pp. 15220-15223, Nov. 2024.

[5] Y. Gui, K. Nainar, J. and D. Bendtsen *et al*., "Voltage support with PV inverters in low-voltage distribution networks: an overview," *IEEE Journal of Emerging and Selected Topics in Power Electronics*, vol. 12, no. 2, pp. 1503-1522, Apr. 2023.

[6] H. Xu, C. Yu, and F. Mao *et al*., "A power oscillation damping algorithm of distributed generators based on optimized second-order virtual inertia," in *2021 IEEE 12th Energy Conversion Congress & Exposition-Asia (ECCE-Asia)*, Singapore, Singapore, May 2021.

[7] J. Wang, R. Wang, and Y. Hu *et al*., "Calculation method for critical permeability of inverter power supply considering instantaneous overcurrent protection," in *2023 4th International Conference on Advanced Electrical and Energy Systems (AEES)*, Shanghai, China, Dec. 2023.

[8] M. Li, X. Zhang, and Z. Guo *et al*., "Impedance adaptive dual-mode control of grid-connected inverters with large fluctuation of SCR and its stability analysis based on D-partition method," *IEEE Transactions on Power Electronics*, vol. 36, no. 12, pp. 14420-14435, Dec. 2021.

[9] Y. Wang and B. Yang, "Optimal PV array reconfiguration under partial shading condition through dynamic leader based collective intelligence," *Protection and Control of Modern Power Systems*, vol. 8, no. 3, pp. 1-16, Jul. 2023.

[10] Y. Wang, X. Wang, and F. Blaabjerg *et al*., "Harmonic instability assessment using state-space modeling and participation analysis in inverter-fed power systems," *IEEE Transactions on Industrial Electronics*, vol. 64, no. 1, pp. 806-816, Jan. 2016.

[11] J. Sun, "Impedance-based stability criterion for grid-connected inverters," *IEEE Transactions on Power Electronics*, vol. 26, no. 11. pp. 3075-3078, Nov. 2011.

[12] W. Wu, L. Zhou, and Y. Chen *et al*., "Sequence-impedance-based stability comparison between VSGs and traditional grid-connected inverters," *IEEE Transactions on Power Electronics*, vol. 34, no. 1, pp. 46-52, Jan. 2018.

[13] W. Yan, S, Shah, and V. Gevorgian *et al*., "Sequence impedance modeling of grid-forming inverters," in *2021 IEEE Power & Energy Society General Meeting (PESGM)*, Washington, DC, USA, Jul. 2021.

[14] C. Yu, H. Xu, C. Liu *et al*., "Research on modeling, stability and dynamic characteristics of voltage-controlled grid-connected energy storage inverters under high penetration," *International Journal of Electrical Power & Energy Systems*, vol. 143, Dec. 2022.

[15] Z. Li, M. Zhu, and C. Hou *et al*., "Impedance modelling mechanisms and stability issues of single phase inverter with SISO structure and frequency coupling effect," *IEEE Transactions on Energy Conversion*, vol. 37, no. 1, pp. 573-584, Jan. 2021.

[16] A. Rygg, M. Molinas, and C. Zhang *et al*., "A modified sequence-domain impedance definition and its equivalence to the *dq*-domain impedance definition for the stability analysis of AC power electronic systems," *IEEE Journal of Emerging and Selected Topics in Power Electronics*, vol. 4, no. 4, pp. 1383-1396, Dec. 2016.

[17] P. Ezhilvannan, S. Krishnan, and B. H. Kumar *et al*., "Analysis of the effectiveness of a two-stage three-phase grid-connected inverter for photovoltaic applications," *Journal of Solar Energy Research*, vol. 8, no. 2, pp. 1471-1483, Mar. 2023.

[18] J. Lin, M. Su, and Y. Sun *et al*., "Frequency coupling suppression control strategy for single-phase grid-tied

inverters in weak grid," *IEEE Transactions on Industrial Electronics*, vol. 69, no. 9, pp. 8926-8938, Sept. 2021.

[19] Z. Xie, Y. Chen, and W. Wu *et al*., "Admittance modeling and stability analysis of grid-connected inverter with LADRC-PLL," *IEEE Transactions on Industrial Electronics,* vol. 68, no. 12, pp. 12272-12284, Dec. 2020.

[20] M. Li, X. Zhang, and Z. Guo *et al*., "The control strategy for the grid-connected inverter through impedance reshaping in q-axis and its stability analysis under a weak grid," *IEEE Journal of Emerging and Selected Topics in Power Electronics, vol.* 9, no. 3, pp. 3229-3242, Mar. 2020.

[21] Z. Xie, Y. Chen, and W. Wu *et al*., "Frequency coupling admittance modeling of quasi-PR controlled inverter and its stability comparative analysis under the weak grid," *IEEE Access*, vol. 9, pp. 94912-94922, Jun. 2021.

[22] S. Song, Z. Wei, and Y. Lin *et al*., "Impedance modeling and stability analysis of PV grid-connected inverter systems considering frequency coupling," *CSEE Journal of Power and Energy Systems*, vol. 6, no. 2, pp. 279-290, Jun. 2020.

[23] N. Fei, H. Xu, and S. Wang, "Frequency-coupling restrained control of PV inverters tied into weak AC grid," in *2020 IEEE Sustainable Power and Energy Conference (iSPEC)*, Chengdu, China, Nov. 2020.

[24] Yu, Changzhou et al. "Modeling and analysis of common-mode resonance in multi-parallel PV string inverters," *IEEE Transactions on Energy Conversion*, vol. 34, no. 1, pp. 446-454, Mar. 2018.

[25] Zhao, Ensheng et al. "Harmonic characteristics and control strategies of grid-connected photovoltaic inverters under weak grid conditions," *International Journal of Electrical Power & Energy Systems*, vol. 142, Nov. 2022.

[26] Y. Wang and B. Yang, "Optimal PV array reconfiguration under partial shading condition through dynamic leader based collective intelligence," *Protection and Control of Modern Power Systems*, vol. 8, no. 3, pp. 1-16, Jul. 2023.

[27] S. K. Kollimalla and M. K. Mishra, "A novel adaptive P&O MPPT algorithm considering sudden changes in the irradiance," *IEEE Transactions on Energy conversion*, vol. 29, no. 3, pp. 602-610, Sept. 2014.

[28] S. Gao, H. Zhao, and Y. Gui *et al*., "Impedance analysis of voltage source converter using direct power control," *IEEE Transactions on Energy Conversion*, vol. 36, no. 2, pp. 831-840, Jun. 2020.

[29] B. Xie, K. Guo, and M. Mao *et al*., "Analysis and improved design of phase compensated proportional resonant controllers for grid-connected inverters in weak grid," *IEEE Transactions on Energy Conversion*, vol. 35, no. 3, Sept. 2020, pp. 1453-1464.

[30] D. Joerg, C. Wessels, and F. W. Fuchs, "Limitations of voltage-oriented PI current control of grid-connected PWM rectifiers with *LCL* filters," *IEEE Transactions on Industrial Electronics*, vol. 56, no. 2, pp. 380-388, Feb. 2008.